Acta Biomaterialia 58 (2017) 492–501

Contents lists available at ScienceDirect

Acta Biomaterialia

journal homepage: www.elsevier.com/locate/actabiomat

Full length article

Toughening of fibrous scaffolds by mobile mineral deposits

Justin Lipner [a,b], John J. Boyle [b], Younan Xia [c], Victor Birman [d], Guy M. Genin [e,b,f,*], Stavros Thomopoulos [g,h,*]

[a] Department of Orthopaedic Surgery, Washington University in St. Louis, St. Louis, MO, USA
[b] Department of Biomedical Engineering, Washington University in St. Louis, St. Louis, MO, USA
[c] The Wallace H. Coulter Department of Biomedical Engineering, Georgia Institute of Technology and Emory University, Atlanta, GA, USA
[d] Department of Mechanical and Aerospace Engineering and Missouri S&T Global – St. Louis, Missouri University of Science and Technology, St. Louis, MO, USA
[e] Department of Mechanical Engineering and Materials Science, Washington University in St. Louis, St. Louis, MO, USA
[f] NSF Science and Technology Center for Engineering MechanoBiology, Washington University in St. Louis, St. Louis, MO, USA
[g] Department of Orthopedic Surgery, Columbia University, New York, NY, USA
[h] Department of Biomedical Engineering, Columbia University, New York, NY, USA

ARTICLE INFO

Article history:
Received 3 January 2017
Received in revised form 10 May 2017
Accepted 15 May 2017
Available online 19 May 2017

Keywords:
Nanofibrous electrospun PLGA scaffolds
Biomineralization
Toughening by mobile mineral
Fracture mechanics
Peel testing
Tendon to bone insertion site
Biomechanics
Enthesis

ABSTRACT

Partially mineralized fibrous tissue situated between tendon and bone is believed to be tougher than either tendon or bone, possibly serving as a compliant, energy absorptive, protective barrier between the two. This tissue does not reform following surgical repair (e.g., rotator cuff tendon-to-bone re-attachment) and might be a factor in the poor outcomes following such surgeries. Towards our long-term goal of tissue engineered solutions to functional tendon-to-bone re-attachment, we tested the hypotheses that partially mineralized fibrous matrices can derive toughness from mobility of mineral along their fibers, and that in such cases toughness is maximized at levels of mineralization sufficiently low to allow substantial mobility. Nanofibrous electrospun poly(lactic–co-glycolic acid) (PLGA) scaffolds mineralized for prescribed times were fabricated as model systems to test these hypotheses. Tensile tests performed at varying angles relative to the dominant fiber direction confirmed that mineral cross-linked PLGA nanofibers without adhering to them. Peel tests revealed that fracture toughness increased with mineralization time up to a peak value, then subsequently decreased with increasing mineralization time back to the baseline toughness of unmineralized scaffolds. These experimental results were predicted by a theoretical model combining mineral growth kinetics with fracture energetics, suggesting that toughness increased with mineralization time until mineral mobility was attenuated by steric hindrance, then returned to baseline levels following the rigid percolation threshold. Results supported our hypotheses, and motivate further study of the roles of mobile mineral particles in toughening the tendon-to-bone attachment.

Statement of significance

Effective surgical repair of interfaces between tendon and bone remains an unmet clinical need, in part due to a lack of understanding of how toughness is achieved in the healthy tissue. Using combined synthesis, experiment, and modeling approaches, the current work supported the hypothesis that toughening of a fibrous scaffold arises from brittle mineral particles that crosslink the fibers, but only if the particles are free to slide relative to the fibers. In the case of the tendon-to-bone interface, this suggests that partially mineralized tissue between tendon and bone, with mobile mineral but relatively low stiffness, may serve as a compliant, energy-absorbing barrier that guards against injury. These results suggest an opportunity for fabrication of tough and strong fibrous scaffolds for tissue engineering applications.

1. Introduction

The attachment of tendon to bone is fascinating as a material system. From a functional perspective, it can resist a lifetime of mechanical loading without succumbing to the stress concentrations that arise at the interface of two dissimilar materials [1,2].

* Corresponding authors at: Department of Mechanical Engineering and Materials Science, Washington University in St. Louis, St. Louis, MO, USA (G.M. Genin), Departments of Orthopedic Surgery and Biomedical Engineering, Columbia University, New York, NY, USA (S. Thomopoulos).
E-mail addresses: genin@wustl.edu (G.M. Genin), sat2@columbia.edu (S. Thomopoulos).

http://dx.doi.org/10.1016/j.actbio.2017.05.033
1742-7061/

From surgical and tissue engineering perspectives, its resilience cannot yet be matched nor regenerated [3–6]. From mechanical and anatomical perspectives, it is at first glance perplexing, with highly ordered tendon devolving into a disordered insertion site [7–9], including competing microstructural factors that combine to produce a partially mineralized tissue that is more compliant than either tendon or bone [10–12]. Although the trade-offs between mineral accrual, collagen organization, and matrix composition that give rise to this compliant tissue are now better understood [10,13,12], the function of this compliant tissue is not [14]. It is clear that the interfacial tissue attenuates stress concentrations [15–17], yet due to its compliance it also amplifies strain [18]. This compliant zone of tissue is believed to be only partially mineralized, and because mobility of mineral at the nanoscale is believed to toughen bone [19], the remarkable toughness of the tendon-to-bone attachment may arise in part from energy resulting from mineral mobility.

Strengthening and toughening of collagenous tissues via hydroxylapatite mineral depends on the location of the mineral relative to the collagen. Mineral inserts both within and atop collagen fibrils in bone, with about half of mineral within and half atop the fibrils [20]. Even in the crowded space between collagen fibrils in bone, non-collagenous proteins (NCPs) binding collagen fibrils to mineral nanocrystals and mineral nanocrystals to one another appear to break and reform, enabling a degree of plasticity and energy absorption in bone [21]. This energy absorption might be accentuated in partially mineralized tissues, in which, at least during development, relatively diffuse clusters of nanocrystals accrue on the exteriors of collagen fibrils [22]. Accumulations of nanocrystals bridging neighboring fibrils have the potential to enhance energy absorption as these mobile mineral-crosslinked fibrils slide relative to one another during deformation.

Mineralized nanofiber material systems, interpreted through theoretical models, are useful for examining fiber-mineral interactions in an idealized setting. In previous studies, mineralized nanofiber scaffolds were synthesized by electrospinning poly(lactic–co-glycolic acid) (PLGA) and mineralizing them using simulated body fluid (SBF) [23,24]. These scaffolds have been developed for a number of musculoskeletal applications, including tendon, ligament, and bone grafting. Previous mechanical characterization experiments on single nanofibers and on network of nanofibers have produced a surprising contradiction: precipitation of calcium phosphate mineral onto nanofiber scaffolds stiffens the scaffolds [24,25] without stiffening or strengthening the individual nanofibers [26]. This counterintuitive result suggests that mineral crystals form structural cross-links between adjacent nanofibers, but do not adhere to the nanofibers, making the system well-suited for testing our hypothesis.

The current study aimed to understand how mineral stiffening and toughening occurs without strengthening the fibers themselves, with the aims of identifying design principles for mineralized nanofiber scaffolds and identifying toughening mechanisms possible in natural, partially mineralized tissues.

We first hypothesized that mineral stiffens and strengthens nanofiber scaffolds predominantly by enhancing links between adjacent fibers. To test this hypothesis and uncover the mechanisms of stiffening, aligned nanofiber scaffolds were tested in tension at a number of off-axis angles. For this experiment, we predicted that the stiffening effect of mineral would be more pronounced in the transverse directions (i.e., perpendicular to the predominant fiber orientation) than in the longitudinal direction (i.e., along the predominant fiber direction). We further predicted that, due to the weak bonding of minerals to fibers, strengthening would occur predominantly in the perpendicular direction. To test the hypothesis that mineral mobility endows scaffolds with toughness, scaffolds were layered, mineralized for prescribed amounts of time, and pulled apart in a peel test configuration. For this experiment, it was predicted that mineral would enhance fracture toughness only at intermediate amounts of mineralization.

2. Methods and materials

2.1. Overview

Two sets of experiments were performed to determine the mechanisms by which mineral stiffens, strengthens, and toughens nanofiber scaffolds. These experiments were interpreted through a series of models that enabled the testing of our hypotheses. The first experiment focused on stiffening and strengthening by mineral by testing aligned mineralized scaffolds at multiple angles relative to the predominant fiber direction. This testing setup revealed the combined effects of mineral stiffening and fiber orientation on scaffold mechanics. The second experiment focused on toughening by mineral by examining fracture energy when peeling one mineralized nanofiber scaffold from a second mineralized nanofiber scaffold. This testing setup specifically isolated the effect of mineral cross bridges on scaffold toughness.

2.2. Off-axis mechanical testing

In earlier work, the effect of fiber alignment and mineral concentration on nanofiber scaffold mechanics was examined only in the direction of fiber alignment (i.e., in the longitudinal direction) [23,24,27]. To examine anisotropy and fiber–fiber interactions, scaffolds must be tested at multiple angles off-axis from the directions of fiber alignment. For example, the mechanical effect of mineral bridges between adjacent nanofibers would be most apparent when scaffolds are tested perpendicular to the direction of fiber alignment.

2.2.1. Scaffold fabrication for off-axis experiments

Electrospinning was performed using the protocol described previously, with several modifications [24]. PLGA (85:15 lactic:glycolic) 50–75 kDa (Sigma, St Louis, MO) was used, dissolved at 25% m/v into 4:1 dichloromethane:N-dimethylformamide (Sigma, St. Louis, MO). The solution was loaded into a 3 mL syringe with a 23.5 ga blunt-end needle and put in a syringe pump, set to release fluid at a rate of 1 mL/hr. The source was set at 18 kV, with a tip-to-collector distance of roughly 23 cm. The mandril rotated at an angular velocity of 1,840 rpm and a linear velocity of roughly 5.8 m/s. Aligned nanofibers were deposited for 1 h. Scaffolds were then mounted to carbon-tape-coated aluminum frames to maintain their size and shape prior to mechanical testing, and samples were cut into two adjacent samples, with one destined to be mineralized. The mounted samples were then plasma treated for 8 min to increase surface energy and hydrophillicity (Harrick Plasma PDC-001) [28]. The frame chosen for mineralization was then mineralized by immersion in 10× SBF (10SBF), set to a pH of 6.6 using sodium bicarbonate, as described in detail previously [25,24]. Due to the high porosity of the scaffolds (~13 vol% polymer), no diffusion limitations were expected for mineralization through the thickness of the samples, but wettability required a lower mandril speed to prevent high fiber density that prevented fluid flow.

2.2.2. Mechanical testing of off-axis samples

Test strips of 3 mm x 15 mm were cut at various angles from the predominant fiber direction (0°, 15°, 30°, 45°, and 90°; Fig. 1), as described by Nerurkar et al. [29], and tested in uniaxial tension under displacement control at a constant strain rate of 0.5%/s. Strain was calculated using a combination of optical and machine outputs. A strain-tracking algorithm was used to determine strain

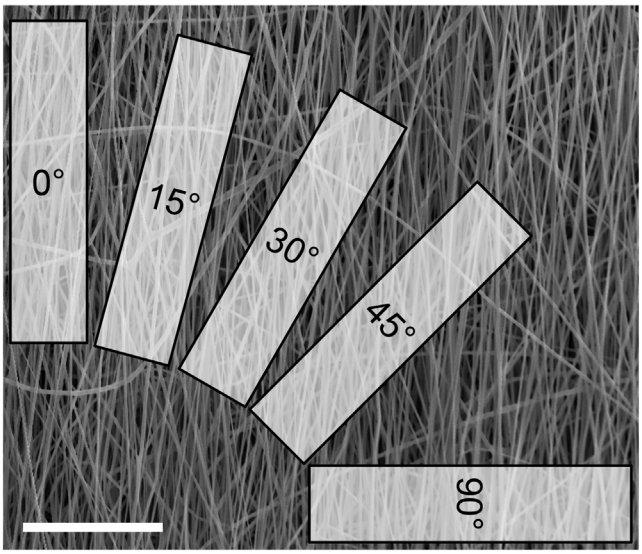

Fig. 1. Test strips (3 mm × 15 mm) were prepared at multiple angles for uniaxial tensile testing (scale bar: 200 μm).

on video captured during testing [30]. The dimensions of the sample were determined from calibrated points on the fixtures. Samples typically failed at the midpoint between the grips; however, 3/62 samples (2/35 in the mineralized group and 1/27 in the unmineralized group) failed at a grip and were excluded from the study. Rectangular-shaped samples were used because of the aligned and fibrous nature of the material; dog-bone shaped samples, which are typically used for tensile tests of solid isotropic materials, are not appropriate for scaffolds consisting of alignment fibrous networks.

2.2.3. Analysis of off-axis mechanical testing

The thickness of the samples was measured using a laser micrometer (Keyence, Nashville, TN) and the width of the samples was measured via calibrated images of the samples and ImageJ (NIH, Bethesda, MD). Load-deformation and stress–strain data was used to determine structural (e.g., stiffness, ultimate load) and material properties (e.g., modulus, strength), respectively.

2.3. Peel test

A more direct method to determine the toughening effect of mineral on fiber–fiber connections is the peel test. Peel tests are used to estimate the fracture energy of an attachment [31–34]. The resistance to peeling is dependent on the fracture energy of the attachment, as a crack forms at the leading edge of the adherents and propagates through the length of the attachment. Using an idealized model developed by Kendall [32] of this testing setup, the fracture energy can then be estimated. This configuration is particularly relevant in the current study to determine the role of mineral cross-bridges between nanofibers on scaffold toughness.

2.3.1. Scaffold fabrication for peel test experiments

A new fabrication method was necessary to create samples suitable for peel test experiments. Aligned nanofibers were electrospun in custom frames, placed perpendicular to each other, and mineralized (Fig. 2). The system was designed using Google SketchUp (Google, Inc. Mountain View, CA) and then fabricated from aluminum sheets and bonded using epoxy (Parson Adhesives, Rochester, MI). This idealized setup was expected to produce welds of mineral at each point where individual perpendicular nanofibers crossed.

Prior to mineralization, aligned PLGA nanofibers were electrospun across the gaps of the two frames (Fig. 2A). Samples were then plasma treated for 4 min to increase surface energy and hydrophillicity (Harrick Plasma PDC-001) [28]. Nanofibers were further secured to the frames using tape to prevent grip failure during peel tests. The width of the nanofiber mat in one frame (Fig. 2, light gray frame) was reduced to roughly 1/3 the width of the nanofiber mat in the second frame (Fig. 2, dark gray frame); this ensured consistent stress across the peeling pieces during testing. Next, the frames were firmly attached at a 90° angle and placed in a container with the frames in a vertical configuration (to prevent mineral precipitates from settling onto the mats). The container was then filled with 10SBF and nanofibers were mineralized for various amounts of time (5, 15, 30, 60 and 120 min). It was previously shown that mineralization time correlates with mineral content [23]. Mineral morphology was examined using scanning electron microscopy (SEM) and energy dispersive X-ray (EDX).

2.3.2. Mechanical testing for peel tests

Prior to mechanical testing, a random texture was applied to the samples for strain tracking using a diffuse spray of Alizarin Red S (10 mg/ml in ddH2O) from an aerosol bottle. The frames were mounted in the two grips as shown in Fig. 2 and peel tests were performed by pulling the top piece from the bottom piece at an initial angle of 90° at a rate of 0.05 mm/s. During the test, video was recorded from one perspective to determine strain in the scaffolds (Illunis VMV-8M; 8MP, 2.67fps) and from a second perspective (smartphone camera on LG D800; 2MP, 30fps) to determine the angle between the two scaffolds.

2.3.3. Analysis of peel test results

Interpretation of peel tests required analysis of three different data sets: (i) force–displacement from the material testing frame data (ElectroPuls E1000, Instron), used to measure the force necessary to separate adherents, (ii) high resolution, low speed video (illunis VMV-8M; 8MP, 2.67fps), used to measure deformation in the samples, and (iii) low resolution, high speed video (smartphone camera on LG D800; 2MP, 30fps), used to measure the angle between the adherents. The three data sets were synchronized using an LED which turned on at the onset of the test. Data were analyzed using custom scripts in MATLAB (Mathworks, Natick, MA). Sample width was measured using ImageJ (NIH, Bethesda, MD) from the neutral images taken prior to the start of the test and calibrated based on known lengths of apparatus segments. The force data was smoothed with an adaptive Savitz-Golay filter.

The Kendall [32] model was used to estimate the fracture toughness G_c from peel test data (Fig. 2):

$$G_c = \frac{F^2}{2w^2 d\,E} + \frac{F}{w}(1 - \cos\varphi) \quad (1)$$

where G_c is the work per unit crack length required to advance the crack, F is the force applied during crack extension, d is the thickness of the peeled portion of the scaffold, w is the depth of the peeled scaffold (distance into the page in Fig. 2C), E is the elastic modulus of the peeled scaffold, and φ is the angle of peeling. The first term on the right-hand side accounts for elasticity of the specimen; as is appropriate for our thin specimens, flexural terms were neglected [35]. The two videos were reviewed simultaneously with the force data to identify when the following idealized criteria for the Kendall [32] model were met: (i) constant peeling velocity, (ii) constant peeling force, (iii) consistent geometry of the peeling strip, and (iv) known angle between adherents. SEM was performed

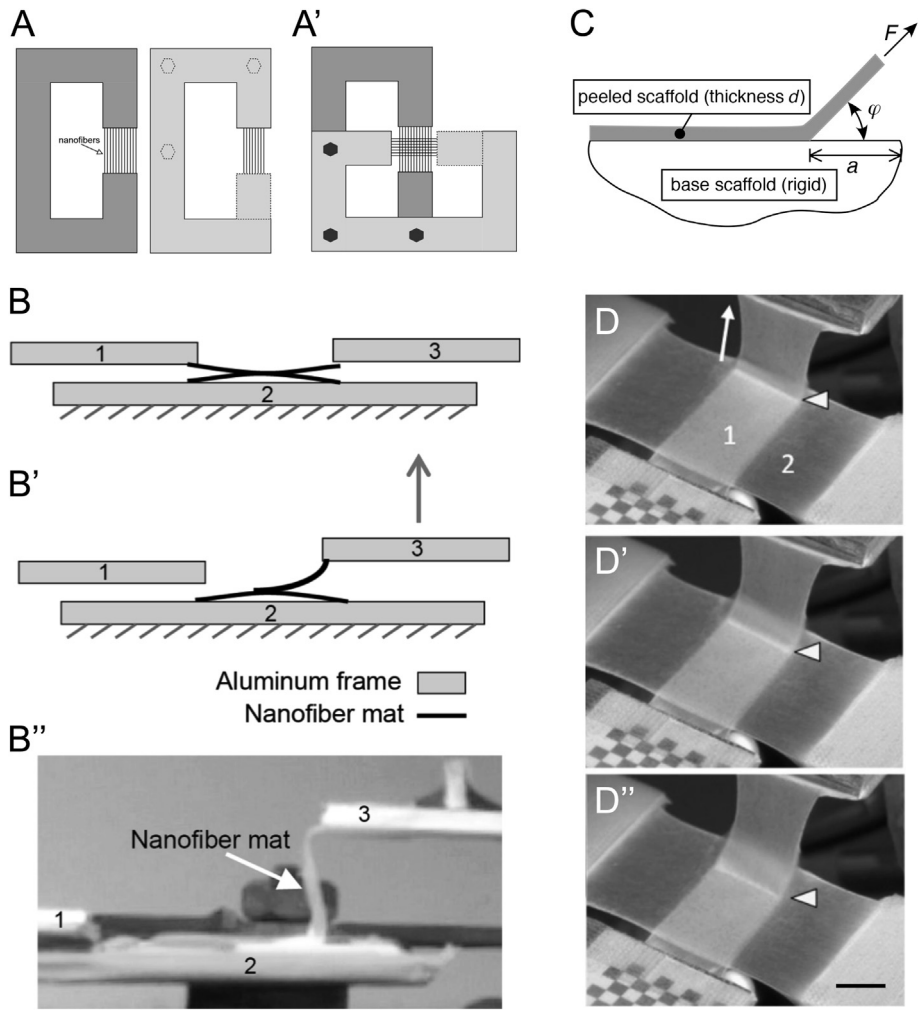

Fig. 2. Fabrication and testing methods for peel test experiments. (A) Peel test samples (top view) were synthesized by first depositing aligned PLGA nanofibers onto two identical frames. Note that the box outlined with a dashed line was detachable, and was removed for mechanical testing. (A′) After electrospinning, one frame was rotated 90° and attached using three bolts (solid black circles). The two layered scaffolds, aligned perpendicular to each other, were then submerged in 10SBF for mineralization. (B) After mounting, the top piece was cut on the left (non-peeling) side at its attachment to frame piece 1 (side view). The right side (piece 3) was then pulled vertically (gray arrow) to create a peeling angle of ~ 90°. (C) A schematic depicting the variables in the Kendall peel test model is shown. Note that elastic energy stored in the lower layer was neglected in the analyses due to its relatively shorter length. (D) Start, middle, and end of a test (direction of displacement is shown by white arrow). The nanofiber mats are labeled 1 and 2, and the arrowhead indicates the crack front. Scale bar: 5 mm.

on some samples to estimate fiber alignment and fiber–fiber bond density (FEI NanoSEM, FEI, Hillsboro, OR).

2.4. Theory

Mathematical models were developed and applied to interpret the experimental observations and test the hypotheses. Three sets of models were needed: first, a multiscale model of how toughening by mobile mineral varies with time of mineralization; second, multiscale models of how scaffold modulus varies with the direction of loading; and third, a phenomenological model of how strength varies with the direction of loading. Details for these models can be found in Appendix A.

2.5. Statistics

To compare mechanical property outcomes, a two-way analysis of variance (ANOVA) was performed for off-axis experiments and a one-way ANOVA was performed for peel tests experiments, followed by post hoc Tukey tests. Significance was set at $p < 0.05$.

3. Results

3.1. Mineral increased the elastic modulus and strength of scaffolds in the direction transverse to the fibers

The effect of mineral on the mechanics of nanofibrous scaffolds was evident from representative stress–strain curves from tensile testing experiments (Fig. 3). These curves showed a small initial non-linear toe region, followed by an elastic region though 0.025 strain and a long plastic deformation plateau region through up to 1.0 strain prior to failure.

In both mineralized and unmineralized scaffolds, a significant effect of testing angle on the strength (ultimate stress) and modulus was evident (Fig. 4), with transverse values always lower than longitudinal values. The modulus and strength of mineralized scaffolds were generally higher, with several notable exceptions. Both the testing angle and the mineral content affected the strength (ultimate stress) and modulus significantly, with transverse values being lower than longitudinal values, mineralization leading to higher modulus, and increasing angle leading to lower strength and modulus (Fig. 4). For both the mineralized and unmineralized

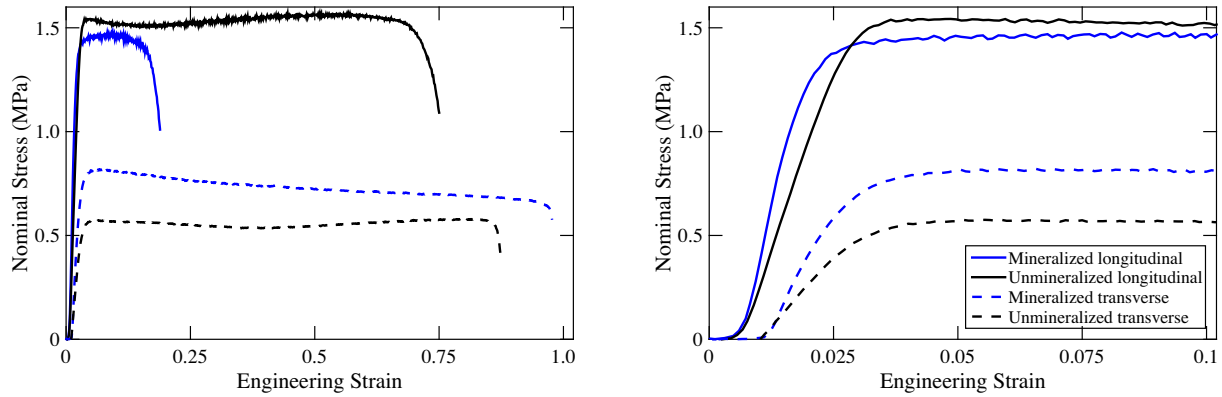

Fig. 3. Representative stress–strain data for mineralized and unmineralized scaffolds loaded parallel (longitudinal) and perpendicular (transverse) to the dominant directions of fibers. Complete stress–strain curves are shown on the left and the same curves through a strain of 0.1 are shown on the right.

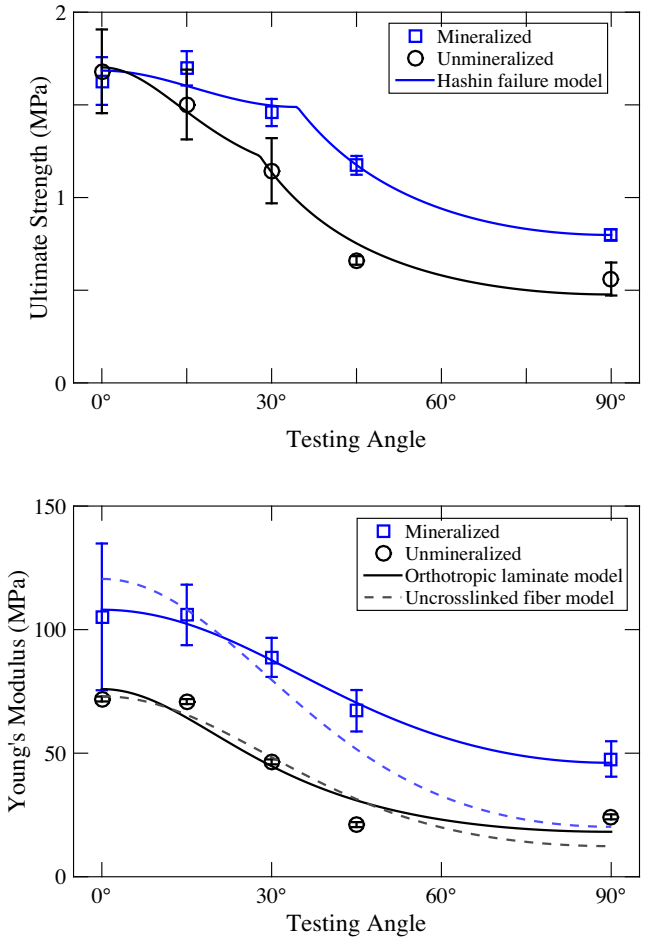

Fig. 4. (Top) Testing angle and mineralization had significant effects on the strength of scaffolds. Strength dropped according to a commonly applied failure criterion for a composite lamina. At low testing angle, the failure mechanism was fiber failure; at higher angles (following the kinks in the curves), the failure mechanism was breakage of connections between fibers. Although mineral did not strengthen fibers, it did strengthen connections between fibers. (Data: mean ± SD). (Bottom) Testing angle and mineralization had significant effects on scaffold modulus. Both mineralized and unmineralized scaffolds behaved more like cohesive orthotropic laminae (solid lines) than like uncrosslinked bundles of fibers (dashed lines). Note that the dashed line for the unmineralized scaffold is based upon fits for both the amplitude and dispersion in Eq. 15, whereas the dashed line for the mineralized scaffold is based upon the structural parameter, b, measured for the unmineralized scaffold, and a fit for the amplitude. (Data: mean ± SD).

samples, scaffolds had the highest strength in the longitudinal direction (0°), with strength dropping significantly by 15° and continuing to drop with increased angle. The addition of mineral led to significantly increased strength only at angles above 30°, with the maximum effect seen at 45°. Strength in the transverse direction was increased ~25% with the addition of mineral whereas it had no effect on the strength in the longitudinal direction.

When examining scaffold factors on modulus, mineralization led to increases at all angles, with the maximum effect at 45° (~100% change). The modulus in the transverse direction was nearly doubled with the addition mineral, but longitudinal modulus was only modestly affected. Specifically, mineral stiffened scaffolds tested at 0°, 15°, 30°, 45°, and 90° by 46%, 49%, 91%, 218%, and 97%, respectively. In absolute terms, however, stiffening effects were similar for all directions tested. Specifically, mineral stiffened scaffolds tested at 0°, 15°, 30°, 45°, and 90° by 33 MPa, 35 MPa, 42 MPa, 46 MPa, and 23 MPa, respectively.

3.2. Low levels of mineralization increased scaffold toughness, but these gains were lost at higher levels of mineralization

Peel test experiments (Fig. 2) demonstrated that mineral significantly increased adhesion energy for groups that were mineralized for up to 30 min, with the trend reversing for 60 and 120 min of mineralization (Fig. 5). The peak toughness was significantly greater than those at other timepoints ($p < 0.005$). SEM combined with EDX was used to examine the morphology and content for each group. Mineral was not observed in the 5 min group, and this group had similar adhesion fracture energy to the 0 min (i.e., unmineralized control) group. Mineralization time had a significant effect on the adhesion fracture energy. Between-group statistical comparisons revealed that adhesion energy was significantly higher with 30 min of mineralization than in all other groups with the exception of 15 min. This indicates that adhesion energy was similar between the highest and lowest mineralization groups, but that 30 min led to increased adhesion.

4. Discussion

4.1. Mineral cross-linked adjacent nanofibers but did not adhere significantly to individual nanofibers

Mechanical characterization of partially mineralized nanofiber scaffolds demonstrated the hallmarks of mobile mineral that cross-linked but did not otherwise adhere strongly to the nanofibers. This was first evident from tensile loading tests of scaffolds in the dominant fiber direction, in which the strength was

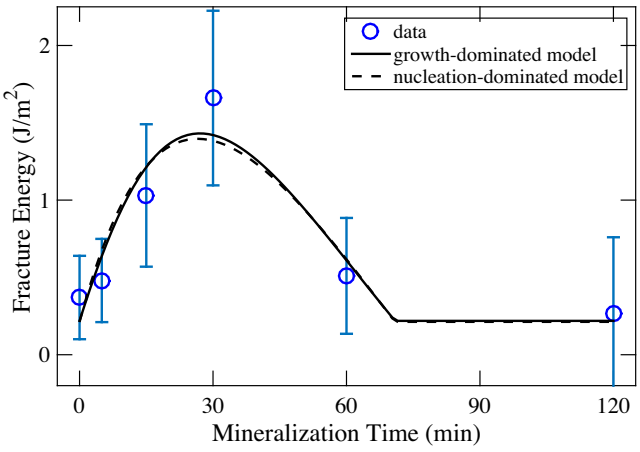

Fig. 5. Very low levels of mineralization did not affect adhesion (0 vs. 5 min), but higher levels of mineralization (30 min) increased peeling fracture energy. At the highest levels of mineralization (60 and 120 min), fracture energy dropped to levels comparable to those of unmineralized samples. (Data: mean ± SD; the peak toughness was significantly greater than those at other timepoints, with $p < 0.005$). The variation of fracture energy with respect to mineralization time was predicted by a model of mineral sliding arrested by rigid percolation (change in slope near $t = 60$ minutes). The two extreme cases considered produced nearly identical predictions.

unaffected by mineral (Fig. 4), indicating that the mineral had ceased to interact mechanically with the scaffold at the point at which failure occurred. However, the strength for tensile loading of scaffolds at angles skew and perpendicular to the fiber directions increased with increasing mineral content, indicating that the mineral enabled improved transfer of load laterally, consistent with an effect of crosslinking. Fitting the Hashin [36] quadratic failure model to the mineralized and unmineralized scaffold data showed a transition in failure mode as a function of loading angle. Fiber failure dominated at low loading angles, while matrix failure dominated at loading angles greater than approximately 30° from the fiber direction; this transition is evident from a kink in the strength versus loading angle curves (Fig. 4).

Consistent with mineral sliding, the tensile strength for loading parallel to the fibers was not affected by mineralization. For loading directions in which fiber failure dominated, mineral likely cracked away without contributing to ultimate strength, as seen previously in single fiber mechanical testing [26]. As shear and transverse loading began to dominate the failure at higher loading angles, effects of crosslinking by mineral became evident, with mineralization increasing fiber–fiber bonding. This was evidenced by the best-fit values of the Hashin quadratic failure model: σ^c_{11}, which corresponds to strength in the dominant direction of the fibers, did not change from 1.7 MPa when the scaffolds were mineralized; σ^c_{22}, which corresponds to strength perpendicular to the dominant direction of the fibers, rose due to cross-linking from 0.48 to 0.80 MPa; σ^c_{12}, which corresponds to shear, rose from 0.61 to 0.87 MPa.

Crosslinking was evident in the results of stiffness measurements performed on both the unmineralized and mineralized scaffolds. Note that these moduli were estimated at a strain level far below failure. In the unmineralized scaffolds, a laminate-like character was evident from a comparison of the direction-dependence of the modulus to two models. The first was the model of a non-cross-linked non-woven fiber assemblage. Fitting this model to the data for the unmineralized specimens, taking the aspect ratio of the specimens as $L/w = 10$, provided a reasonable scaling for the lower testing angles, but a less adequate fit for the capture the response of the unmineralized specimens to loading perpendicular to the dominant direction of the fibers. This suggested that a small degree of cross-linking (or perhaps fiber entanglement) was likely present.

Taking the best-fit dispersion value of $b = 0.94$ found for the unmineralized scaffold and applying it to fit the model for uncross-linked fibers to the mechanics of the mineralized scaffold led to a poor fit. Particularly notable was the poor fit for high loading angles. The mineral accumulations caused the angle-dependent moduli of the scaffold to drift further from that expected from a mat of uncrosslinked fibers, indicating that mineral cross-linked the fibers.

For both the mineralized and unmineralized scaffolds, a reasonable fit to the angle-dependent moduli could be obtained the orthotropic laminate model (Fig. 4). The ratio E_{90}/E_0, a metric of the degree of cross-linking, increased from 0.30 to 0.48 with mineralization, indicating once again that mineral cross-linked the fibers. The increase in E_0 from 80 to 110 MPa with mineralization was not associated with a strengthening of the scaffold, indicating that the mineral was no longer functioning in the direction of the fibers at the point of failure. Combined with the observations of Kolluru et al. that mineralization does not stiffen individual fibers [26], this suggested a role of crosslinking in increasing scaffold modulus. Furthermore, the increase in E_{90} from 24 to 53 MPa was associated with an increase in σ^c_{22} from 0.48 to 0.80 MPa, indicating that mineral contributed to the mechanics of the scaffolds transverse to the fibers up to the point of failure.

The current studies support the hypothesis that mineral stiffening of nanofiber scaffolds occurs via increased connections between fibers. In a previous publication, unmineralized aligned nanofiber scaffolds were tested at various angles, demonstrating similar outcomes to those of the mineralized scaffolds in the current study [29]. Here, we also showed that mineralization stiffened the scaffolds at all test directions, and most strongly at 45° to the fiber direction. At this testing angle, nanofibers were neither aligned with the direction of load (which would provide the highest resistance) nor perpendicular to the direction of load (which would provide the least resistance). The observed effect of mineral at this testing angle suggests that it provides resistance to fiber realignment under loading.

4.2. Mobile mineral toughened scaffolds up to a percolation threshold

Peel tests of layered, mineralized, nanofiber scaffolds showed that even a relatively low level of mineral significantly increased bonding between nanofibers. Furthermore, the effect was dose-dependent, with increased mineralization leading to higher fracture energy, although the trend reversed at the highest mineral concentrations. The strong effect of mineral on adhesive strength between fibers also supported the hypothesis that mineral bridges and bonds neighboring fibers.

Mineral and PLGA are mechanically dissimilar: the mineral is stiff and brittle, and the PLGA is compliant and ductile. In the scaffolds considered here, the polymer fraction was kept constant and mineral was added. Liu et al. demonstrated that when modified 10SBF was used to mineralize PLGA nanofiber scaffolds, the modulus rose as the toughness fell [27]. However, in our experiments, the addition of small amounts of brittle mineral *toughened* the scaffolds, while at the highest concentrations of mineral, the peeling fracture energy was reduced to that of the unmineralized case.

These seemingly contradictory results supported our hypothesis that mineral formed a loosely adherent layer on these scaffolds and contributed to scaffold mechanics exclusively by crosslinking scaffold fibers with sliding connections. The two bounding cases modeled produced nearly indistinguishable predictions when fit to our data, and predicted the data reasonably (Fig. 5). The point

of percolation was overpredicted by a few percent in our model, perhaps indicating a role of shape, orientation, or heterogeneity of the mineral accumulations, or perhaps indicating a relatively minor role for lock-up of mineral sliding occurring at crosslinks between fibers that existed prior to mineralization. The scissoring of these scaffolds into the direction of loading can lead to substantial Poisson contraction [37]. The contribution of G_a to the fracture toughness of adhesion between fibers was similar for both low and high degrees of mineralization. Sources of this baseline toughness include adhesion and entanglement of the nanofibers. This implies that mineral fracture did not contribute significantly to the overall fracture toughness of the scaffolds, and suggests that mineralization has little effect on the adhesion between fibers.

Both models of mineral sliding (growth-dominated and nucleation-dominated) produced trends that matched the input data (Fig. 5). The inputs to the model were G_a and G_s^{max} along with best-fit time constants predicting that the peak fracture energy was reached at 27 min of mineralization. The remainder of the trends were predictive of the data, including the shape of the rise and fall in fracture energy with mineralization time and the ratio of the time of peak sliding contribution to the time of percolation at which this contribution disappeared.

4.3. Further tailoring of toughening by a brittle mineral matrix is possible

The material system we studied here falls into a larger category of brittle matrix fibrous composite materials that can be toughened by frictional sliding between fibers and matrix. Such materials include ceramic matrix laminates developed for high temperature applications with strong fibers that maintain integrity as a brittle matrix cracks away [38,39]. Here, the interface between fibers and matrix is designed to attract and arrest growing cracks [40,41], and the composite eventually fails as the fibers fracture and slide against the matrix [42,43]. Although, unlike the material we studied here, cracking of the ceramic matrix of an engineering composite absorbs substantial energy, some insight can be gained from the fact that both materials absorb substantial energy as fibers slide against and pull out from the matrix [44]. From a macrostructural perspective, these processes transform the system of brittle matrix and brittle fibers into a ductile composite [45–48]. From the microstructural perspective, the tunable details of the fiber–matrix interactions are key determinants of toughness [45].

The interactions between collagen and mineral are now believed to be central to the toughness of bone. The hypothesis that mobile mineral absorbs energy in bone and developing bone was advanced numerically by the Buehler group [19,49–51]. These first-principle and coarse-grained simulations show that interactions between mineral and collagen dominate this toughening phenomenon. In the current study, our system was relatively simple, with friction between PLGA and mineral governing interactions. Based on tensile tests, mineralization of nanofiber scaffolds caused an approximately 2-fold increase in strength and no consistent change in toughness. Based on peel tests, optimal levels of mineralization led to an approximately 5-fold increase in toughness. The Buehler group's modeling study also showed a 2-fold increase in strength and a 5-fold increase in toughness, generally consistent with our experimental results. Nevertheless, the two studies differ in approach (model vs. experiment) and the nature of the fibers (collagen with intrafibrillar mineral vs. PLGA with extrafibrillar mineral). Despite these differences, the key questions are: what degree of tailoring of these interactions is possible, and how can our results be translated to bone and partially mineralized natural tissues?

In bone, the Thurner group has put forth a hypothesis that NCPs, especially osteopontin and osteocalcin, mediate the interactions between collagen and mineral [21]. These interactions are mediated by charge condensation and shared ionic bonds that are controlled by divalent cations interacting with the long disordered chains of the NCPs [52,53]. Support for this hypothesis comes from the dominant presence of NCPs on bone fracture surfaces [54] and from the close relationship between osteopontin efficiency and osteoporotic pathology [55,56]. From this perspective, the reconstitution of this class of toughening is particularly compelling for a number of reasons. First, dissipation coming from interrupting these ionic bonds during sliding is, unlike our current model system, recoverable: after stressing is released, the bonds can reform and pull mineral back to a state in which sliding-based dissipation can again occur. Second, the nature of NCPs enables the possibility of tuning sliding stresses. Finally, when combined with the nanoscale size and irregular spatial distribution of mineral around collagen in partially mineralized tissues [20,22], it enables a relatively large amount of toughening per unit mineral volume.

The model system studied here does not enable the easy binding of NCPs, but should be tunable to a degree. In a previous study, chitosan and heparin were attached to PLGA nanofibers to explore improved mechanical connection between the mineral crystals and the nanofibers, and the stiffening effect of the mineral was more potent [24]. Surface treatments like these could be a useful method to improve mineral bridge adhesion strength. Additionally, the morphology of the mineral can change the mineral-polymer bond area and also the apparent modulus of the mineral. Previous work demonstrated that mineral morphology can be changed dramatically with small changes in mineralizing fluid composition, and that mineral coatings with smaller particles had a more potent stiffening effect on the scaffolds [24].

Although the current results supported the initial hypothesis, current approaches for stiffening PLGA nanofiber scaffolds produce materials that are at least an order-of-magnitude weaker than bone and bony interface applications. Thus, improvements must be made to this material system for it to approximate the properties of natural mineralized tissues. The results of the current experiments provide insight into the stiffening effects of mineral on nanofiber scaffolds, and methods to test these effects.

5. Conclusions

This work provides support for the hypothesis that mobile mineral deposits can toughen fibrous scaffolds at concentrations of mineral that enable energy absorption through mineral sliding. The system we developed enabled mobile mineral to be added to a scaffold without strengthening the scaffold. Although this mineral is known to reduce the toughness of individual PLGA fibers, the mineral toughened a fibrous PLGA scaffold for intermediate but not long mineralization times. These results are consistent with a multiscale model combining nucleation kinetics with the energetics of fracture. The loss in toughening occurred due to a loss in mineral mobility that occurred as the mineral depositions approached rigid percolation. Results show significant toughening of fibrous materials by mobile mineral deposits, and point to opportunities to optimize toughening of fibrous scaffolds for engineering and surgical use by tailoring mineral/nanofiber interactions. Mineralized scaffolds like the ones presented in this work have potential applications in clinical practice, particularly for bone and tendon-to-bone applications.

Acknowledgments

This work was supported in part by the NIH through grant R01 AR060820, by the NSF and NIH through grant U01 EB016422, and

by the NSF through the Science and Technology Center for Engineering MechanoBiology grant CMMI 1548571.

Appendix A. Appendix – Theory

A.1. Multiscale model of the effect of mineralization time on scaffold toughening

The first model relates the time that a scaffold was immersed in the mineralizing solution to the toughness of the scaffold. The model consists of two parts. The first relates the amount of mobile mineral to the degree of sliding and hence energy absorption by the mineral particle. The particle itself is treated as brittle and of appreciable strength but negligible fracture toughness. The second relates the time of mineralization to the volume fraction and spatial disposition of mineral.

A.1.1. Toughening by mineral sliding

The energy release rate G_c is the sum of that associated with adhesion, G_a, and that associated with sliding, G_s:

$$G_c = G_a + G_s \tag{2}$$

As described in the results section, our data indicated a baseline value of $G_a \approx 0.3\,\mathrm{J/m^2}$ for the case of no mineralization, and an addition due to sliding $0 \leqslant G_s^{max} \approx 1.4\,\mathrm{J/m^2}$ that depended on the duration of mineralization (Fig. 5). Because the data showed that toughening was highest for intermediate durations of mineralization, we developed a model to quantify how sliding of mineral would vary with the duration of mineralization, and to quantify the associated energetics of toughening.

Measured force–displacement curves indicated that the crack advanced in increments $a \approx$1–2 mm, and the videos indicated a predominantly mode I crack (Fig. 2B). The increment of work δU associated with the sliding of mineral as such a crack advances a distance δa is:

$$\delta U = \sum_{i=1}^{N} \Delta_i D = \Delta_m D(\rho w\, \delta a) \tag{3}$$

where N is the number of sliding mineral connections in a region of length a and width w, ρ is the areal number density of such sliding elements, D is the average drag force during sliding, and Δ_i is the sliding distance of element i during the process of fracture, with mean Δ_m. The energy release rate G_s is:

$$G_s = \frac{1}{w}\frac{\partial U}{\partial a} = \rho D\left(a\frac{\partial \Delta_m}{\partial a} + \Delta_m\right) \tag{4}$$

The sliding distance decreases with the number and size (mean area in the plane of the scaffold, A_m) of the sliding elements down to the point of rigid percolation:

$$\Delta_m = \begin{cases} \left(1 - \frac{\rho}{\phi}A_m\right)a, & 0 \leqslant \frac{\rho}{\phi}A_m \leqslant 1 \\ 0, & \frac{\rho}{\phi}A_m \geqslant 1 \end{cases} \tag{5}$$

where $\phi \approx 0.65$ is the area fraction associated with percolation, so that:

$$\frac{\partial \Delta_m}{\partial a} = \begin{cases} \left(1 - \frac{\rho}{\phi}A_m\right) - \frac{a}{\phi}\frac{\partial}{\partial a}(\rho A_m), & 0 \leqslant \frac{\rho}{\phi}A_m \leqslant 1 \\ 0, & \frac{\rho}{\phi}A_m \geqslant 1 \end{cases} \tag{6}$$

A.1.2. The effect of mineralization time on toughening

The effect of mineralization time on toughening enters the model through the rate and disposition of mineral. The two extreme cases were considered for estimation of $\partial(\rho A_m)/\partial a$: nucleation- and the growth-dominated cases.

Nucleation-dominated model. In the first extreme, the process of mineral nucleation is the rate limiting phenomenon, and mineral accumulations reach a stable area A_m immediately upon nucleation. Assuming first-order reaction kinetics with rate constant k_N, the density of nuclei scales as [57]:

$$\rho = \frac{1}{A_m}(1 - \exp(-k_N t)) \tag{7}$$

and the second term in Eq. (6) vanishes. In this case, for $0 \leqslant \frac{\rho}{\phi}A_m \leqslant 1$,

$$\frac{\partial \Delta_m}{\partial a} = 1 - \frac{1}{\phi}(1 - \exp(-k_N t)) \tag{8}$$

Thus, for the nucleation-dominated case, over the time interval $0 \leqslant t \leqslant -(1/k_N)\ln(1-\phi)$,

$$G_s^N = G_s^{max}\frac{4}{\phi}\left(1 - \exp(-k_N t) - \frac{1}{\phi}(1 - \exp(-k_N t))^2\right) \tag{9}$$

where $G_s^{max} = \phi D a/2A_m$, and 0 for all other t. The maximum occurs at time $t = (-1/k_N)\ln(1 - (\phi/2))$.

Growth-dominated model. In the other extreme, nucleation is a rare event and the radii of nuclei increase following first-order reaction kinetics [57]:

$$R_{mean} = R_{max}(1 - \exp(-k_G t)) \tag{10}$$

or

$$A_m = \frac{1}{\rho}(1 - \exp(-k_G t))^2 \tag{11}$$

where $1/\rho$ is the limit for A_m as the entire area becomes mineralized. In this case as well, the second term in Eq. (6) vanishes. Thus, for $0 \leqslant \frac{\rho}{\phi}A_m \leqslant 1$,

$$\frac{\partial \Delta_m}{\partial a} = 1 - \frac{1}{\phi}(1 - \exp(-k_G t))^2 \tag{12}$$

The drag force scales with the diameter of the mineral deposits, so that:

$$D = D_{max}(1 - \exp(-k_G t)) \tag{13}$$

Thus, in the growth-dominated case, over the time interval $0 \leqslant t \leqslant -(1/k_G)\ln(1-\phi)$,

$$G_s^G = G_s^{max}\left(\frac{3\sqrt{3\phi}}{2\phi}\right)\left(1 - \exp(-k_G t) - \frac{1}{\phi}(1 - \exp(-k_G t))^3\right) \tag{14}$$

where $G_s^{max} = (4\sqrt{3\phi})\rho a D_{max}/9$, and 0 for all other t. The maximum occurs at $t = (-1/k_G)\ln(1 - \sqrt{\phi/3})$.

A.2. Multiscale models of how scaffold modulus varies with direction of loading

Multiscale models of scaffold modulus were developed to help determine the degree to which mineral adhered to or crosslinked the nanofibers. Two models were considered: first, a non-crosslinked, non-woven fiber assemblage model; and second, a standard orthotropic laminate model.

Non-crosslinked, non-woven fiber assemblage model. A broad range of models exists for the modulus of an assemblage of non-crosslinked, non-woven fibers [58–62]. We applied such models to predict the direction-dependent response of a scaffold clamped and stretched at an angle θ_0 to the dominant direction. The simplest involves non-interacting fibers:

$$E(\theta_0) = C\int_{-\theta_{lim}}^{+\theta_{lim}} p(\theta|\theta_0, b)\cos^3\theta d\theta \tag{15}$$

where C is a constant to be fitted and $p(\theta)d\theta$ is the probability of finding a fiber oriented between θ to $\theta + d\theta$, assigned according to a von Mises distribution [63]:

$$p(\theta|\theta_0, b) = \frac{e^{b\cos(2(\theta-\theta_0))}}{\pi I_0(b)} \tag{16}$$

in which $1/b$ is a measure of the dispersion of the fiber distribution. The fibers that contribute to the resistance to stretching lie within $-\theta_{lim} \leqslant \theta \leqslant +\theta_{lim}$. For the comparison model of interest, only fibers directly clamped by the grips contribute to the modulus, so that $\theta_{lim} = \tan^{-1}(w/L)$, where L is the gauge length of the specimen. The constant C could be written in terms of the mechanics of the individual fibers, if known, as:

$$C = fE_{fiber}\frac{A_{fiber}}{wd} \tag{17}$$

where f, E_{fiber}, and A_{fiber} are the volume fraction, elastic modulus, and cross-sectional area of individual fibers, respectively, and w and d are the width and thickness of the specimen, respectively.

Orthotropic laminate model. For an orthotropic laminate consisting of fibers that deform in registry with an elastic matrix (or, equivalently, a population of fibers undergoing affine deformation), the angle-dependent moduli can be obtained by rotating the stiffness tensor for an orthotropic, linear elastic laminate by the loading angle, θ (Fig. 4) [64]:

$$\frac{1}{E(\theta)} = \frac{1}{E_0}\cos^4(\theta) + \frac{1}{E_{90}}\sin^4(\theta) + S\sin^2(\theta)\cos^2(\theta) \tag{18}$$

where E_0 and E_{90} are the laminate moduli parallel and perpendicular to the dominant fiber direction, and S is a material constant that relates to shear distortion and Poisson contraction. The ratio E_{90}/E_0, is a metric of the relative degree of cross-linking in the scaffolds studied.

A.3. Phenomenological model of how strength varies with the direction of loading

To further assess crosslinking and adhesion of nanofibers, we studied the directional variation of strength in the context of an elementary phenomenological model of symmetric, fibrous, orthotropic laminae. The failure of such laminae is typically characterized by distinct failure loads for uniaxial stressing parallel to the dominant direction of the fibers (σ^c_{11}), uniaxial stressing perpendicular to the dominant direction of the fibers (σ^c_{22}), and shearing in axes aligned with the fibers (σ^c_{12}). A number of schemes exist for predicting failure in response to a general multiaxial loading based upon these quantities. Amongst the simplest of these is the Hashin [36] quadratic failure model, which predicts that an orthotropic, fibrous lamina loaded in tension fails if either of the following are satisfied:

$$\left(\frac{\sigma_{11}}{\sigma^c_{11}}\right)^2 + \left(\frac{\sigma_{12}}{\sigma^c_{12}}\right)^2 = 1 \tag{19}$$

$$\left(\frac{\sigma_{22}}{\sigma^c_{22}}\right)^2 + \left(\frac{\sigma_{12}}{\sigma^c_{12}}\right)^2 = 1 \tag{20}$$

where σ_{ij} are the planar components of the nominal stress tensor applied to the specimen, and the x_1 and x_2 directions are oriented parallel and perpendicular to the dominant fiber directions, respectively.

References

[1] M.M. Tei, K.F. Farraro, S.L.-Y. Woo, Ligament and tendon enthesis: anatomy and mechanics, in: Structural Interfaces and Attachments in Biology, Springer, 2013, pp. 69–89.

[2] S. Thomopoulos, V. Birman, G.M. Genin, The challenge of attaching dissimilar materials, in: Structural Interfaces and Attachments in Biology, Springer, 2013, pp. 3–17.

[3] D.n. Harryman, L. Mack, K. Wang, S. Jackins, M.L. Richardson, F.R. Matsen, Repairs of the rotator cuff. correlation of functional results with integrity of the cuff, J. Bone Joint Surgery 73 (7) (1991) 982–989.

[4] L.M. Galatz, C.M. Ball, S.A. Teefey, W.D. Middleton, K. Yamaguchi, The outcome and repair integrity of completely arthroscopically repaired large and massive rotator cuff tears, J. Bone Joint Surg. Am. 86 (2) (2004) 219–224.

[5] J.S. Dines, D.A. Grande, D.M. Dines, Tissue engineering and rotator cuff tendon healing, J. Shoulder Elbow Surg. 16 (5) (2007) S204–S207.

[6] H.H. Lu, S. Thomopoulos, Functional attachment of soft tissues to bone: development, healing, and tissue engineering, Ann. Rev. Biomed. Eng. 15 (2013) 201.

[7] M. Benjamin, T. Kumai, S. Milz, B. Boszczyk, A. Boszczyk, J. Ralphs, The skeletal attachment of tendons tendon entheses, Comp. Biochem. Physiol. Part A: Mol. Integr. Physiol. 133 (4) (2002) 931–945.

[8] S. Thomopoulos, J.P. Marquez, B. Weinberger, V. Birman, G.M. Genin, Collagen fiber orientation at the tendon to bone insertion and its influence on stress concentrations, J. Biomech. 39 (10) (2006) 1842–1851.

[9] S. Thomopoulos, G.R. Williams, J.A. Gimbel, M. Favata, L.J. Soslowsky, Variation of biomechanical, structural, and compositional properties along the tendon to bone insertion site, J. Orthop. Res. 21 (3) (2003) 413–419.

[10] L.K. Noldner, H.J. Edgar, 3d representation and analysis of enthesis morphology, Am. J. Phys. Anthropol. 152 (3) (2013) 417–424.

[11] G.M. Genin, A. Kent, V. Birman, B. Wopenka, J.D. Pasteris, P.J. Marquez, S. Thomopoulos, Functional grading of mineral and collagen in the attachment of tendon to bone, Biophys. J. 97 (4) (2009) 976–985.

[12] Y. Liu, S. Thomopoulos, C. Chen, V. Birman, M.J. Buehler, G.M. Genin, Modelling the mechanics of partially mineralized collagen fibrils, fibres and tissue, J. R. Soc. Interface 11 (92) (2014) 20130835.

[13] G.M. Genin, V. Birman, Micromechanics and structural response of functionally graded, particulate-matrix, fiber-reinforced composites, Int. J. Solids Struct. 46 (10) (2009) 2136–2150.

[14] Y. Liu, V. Birman, C. Chen, S. Thomopoulos, G.M. Genin, Mechanisms of bimaterial attachment at the interface of tendon to bone, J. Eng. Mater. Technol. 133 (1) (2011) 011006.

[15] M. Benjamin, E. Evans, L. Copp, The histology of tendon attachments to bone in man, J. Anat. 149 (1986) 89.

[16] Y. Liu, S. Thomopoulos, V. Birman, J.-S. Li, G.M. Genin, Bi-material attachment through a compliant interfacial system at the tendon-to-bone insertion site, Mech. Mater. 44 (2012) 83–92.

[17] F. Saadat, V. Birman, S. Thomopoulos, G.M. Genin, Effective elastic properties of a composite containing multiple types of anisotropic ellipsoidal inclusions, with application to the attachment of tendon to bone, J. Mech. Phys. Solids 82 (2015) 367–377.

[18] G.M. Genin, Y. Liu, Models for the mechanics of joining dissimilar materials, in: Structural Interfaces and Attachments in Biology, Springer, 2013, pp. 43–66.

[19] M. Buehler, Molecular nanomechanics of nascent bone: fibrillar toughening by mineralization, Nanotechnology 18 (2007) 295102.

[20] B. Alexander, T.L. Daulton, G.M. Genin, J. Lipner, J.D. Pasteris, B. Wopenka, S. Thomopoulos, The nanometre-scale physiology of bone: steric modelling and scanning transmission electron microscopy of collagen–mineral structure, J. R. Soc. Interface (2012). rsif20110880.

[21] O.L. Katsamenis, T. Jenkins, P.J. Thurner, Toughness and damage susceptibility in human cortical bone is proportional to mechanical inhomogeneity at the osteonal-level, Bone 76 (2015) 158–168.

[22] A.G. Schwartz, J.D. Pasteris, G.M. Genin, T.L. Daulton, S. Thomopoulos, Mineral distributions at the developing tendon enthesis, PLoS One 7 (11) (2012) e48630.

[23] X. Li, J. Xie, J. Lipner, X. Yuan, S. Thomopoulos, Y. Xia, Nanofiber scaffolds with gradations in mineral content for mimicking the tendon-to-bone insertion site, Nano Lett. 9 (7) (2009) 2763–2768.

[24] J. Lipner, W. Liu, Y. Liu, J. Boyle, G.M. Genin, Y. Xia, S. Thomopoulos, The mechanics of PLGA nanofiber scaffolds with biomimetic gradients in mineral for tendon-to-bone repair, J. Mech. Behavior Biomed. Mater. 40 (2014) 59–68.

[25] A.C. Tas, S.B. Bhaduri, Rapid coating of Ti_6Al_4V at room temperature with a calcium phosphate solution similar to 10× simulated body fluid, J. Mater. Res. 19 (09) (2004) 2742–2749.

[26] P.V. Kolluru, J. Lipner, W. Liu, Y. Xia, S. Thomopoulos, G.M. Genin, I. Chasiotis, Strong and tough mineralized plga nanofibers for tendon-to-bone scaffolds, Acta Biomater. 9 (12) (2013) 9442–9450.

[27] W. Liu, Y.-C. Yeh, J. Lipner, J. Xie, H.-W. Sung, S. Thomopoulos, Y. Xia, Enhancing the stiffness of electrospun nanofiber scaffolds with a controlled surface coating and mineralization, Langmuir 27 (15) (2011) 9088–9093.

[28] X. Qu, W. Cui, F. Yang, C. Min, H. Shen, J. Bei, S. Wang, The effect of oxygen plasma pretreatment and incubation in modified simulated body fluids on the formation of bone-like apatite on poly (lactide-co-glycolide)(70/30), Biomaterials 28 (1) (2007) 9–18.

[29] N.L. Nerurkar, D.M. Elliott, R.L. Mauck, Mechanics of oriented electrospun nanofibrous scaffolds for annulus fibrosus tissue engineering, J. Orthop. Res. 25 (8) (2007) 1018–1028.

[30] J.J. Boyle, M. Kume, M.A. Wyczalkowski, L.A. Taber, R.B. Pless, Y. Xia, G.M. Genin, S. Thomopoulos, Simple and accurate methods for quantifying deformation, disruption, and development in biological tissues, J. R. Soc. Interface 11 (100) (2014) 20140685.

[31] A. Gent, G. Hamed, Peel mechanics for an elastic-plastic adherend, J. Appl. Polym. Sci. 21 (10) (1977) 2817–2831.
[32] K. Kendall, Thin-film peeling-the elastic term, J. Phys. D: Appl. Phys. 8 (13) (1975) 1449.
[33] P. Steinmann, H. Hintermann, A review of the mechanical tests for assessment of thin-film adhesion, J. Vacuum Sci. Technol. A 7 (3) (1989) 2267–2272.
[34] J. Williams, Root rotation and plastic work effects in the peel test, J. Adhes. 41 (1–4) (1993) 225–239.
[35] A. Kinloch, C. Lau, J. Williams, The peeling of flexible laminates, Int. J. Fract. 66 (1) (1994) 45–70.
[36] Z. Hashin, Failure criteria for unidirectional fiber composites, J. Appl. Mech. 47 (2) (1980) 329–334.
[37] M.N. Silberstein, C.-L. Pai, G.C. Rutledge, M.C. Boyce, Elastic–plastic behavior of non-woven fibrous mats, J. Mech. Phys. Solids 60 (2) (2012) 295–318.
[38] D.B. Marshall, B.N. Cox, A.G. Evans, The mechanics of matrix cracking in brittle-matrix fiber composites, Acta Metall. 33 (11) (1985) 2013–2021.
[39] E.Y. Luh, A.G. Evans, High-temperature mechanical properties of a ceramic matrix composite, J. Am. Ceram. Soc. 70 (7) (1987) 466–469.
[40] B.N. Cox, F.W. Zok, Advances in ceramic composites reinforced by continuous fibers, Curr. Opin. Solid State Mater. Sci. 1 (5) (1996) 666–673.
[41] A. Evans, F. Zok, The physics and mechanics of fibre-reinforced brittle matrix composites, J. Mater. Sci. 29 (15) (1994) 3857–3896.
[42] Y. Swolfs, R.M. McMeeking, V.P. Rajan, F.W. Zok, I. Verpoest, L. Gorbatikh, Global load-sharing model for unidirectional hybrid fibre-reinforced composites, J. Mech. Phys. Solids 84 (2015) 380–394.
[43] W.A. Curtin, Theory of mechanical properties of ceramic-matrix composites, J. Am. Ceram. Soc. 74 (11) (1991) 2837–2845.
[44] Z.C. Xia, J.W. Hutchinson, A.G. Evans, B. Budiansky, On large scale sliding in fiber-reinforced composites, J. Mech. Phys. Solids 42 (7) (1994) 1139–1158.
[45] B.N. Cox, H.A. Bale, M. Begley, M. Blacklock, B.-C. Do, T. Fast, M. Naderi, M. Novak, V.P. Rajan, R.G. Rinaldi, et al., Stochastic virtual tests for high-temperature ceramic matrix composites, Annu. Rev. Mater. Res. 44 (2014) 479–529.
[46] G.M. Genin, J.W. Hutchinson, Composite laminates in plane stress: constitutive modeling and stress redistribution due to matrix cracking, J. Am. Ceram. Soc. 80 (5) (1997) 1245–1255.
[47] G.M. Genin, J.W. Hutchinson, Failures at attachment holes in brittle matrix laminates, J. Compos. Mater. 33 (17) (1999) 1600–1619.
[48] V.P. Rajan, F.W. Zok, Stress distributions in bluntly-notched ceramic composite laminates, Compos Part A: Appl. Sci. Manuf. 60 (2014) 15–23.
[49] M. Buehler, Y. Yung, Deformation and failure of protein materials in physiologically extreme conditions and disease, Nat. Mater. 8 (3) (2009) 175–188.
[50] M.J. Buehler, G.M. Genin, Integrated multiscale biomaterials experiment and modelling: a perspective, Interface Focus 6 (1) (2016) 20150098.
[51] M. Buehler, T. Ackbarow, Nanomechanical strength mechanisms of hierarchical biological materials and tissues, Comput. Methods Biomech. Biomed. Eng. 11 (6) (2008) 595–607.
[52] G.E. Fantner, J. Adams, P. Turner, P.J. Thurner, L.W. Fisher, P.K. Hansma, Nanoscale ion mediated networks in bone: osteopontin can repeatedly dissipate large amounts of energy, Nano Lett. 7 (8) (2007) 2491–2498.
[53] B. Zappone, P.J. Thurner, J. Adams, G.E. Fantner, P.K. Hansma, Effect of Ca^{2+} ions on the adhesion and mechanical properties of adsorbed layers of human osteopontin, Biophys. J. 95 (6) (2008) 2939–2950.
[54] P.J. Thurner, S. Lam, J.C. Weaver, D.E. Morse, P.K. Hansma, Localization of phosphorylated serine, osteopontin, and bone sialoprotein on bone fracture surfaces, J. Adhes. 85 (8) (2009) 526–545.
[55] P.J. Thurner, C.G. Chen, S. Ionova-Martin, L. Sun, A. Harman, A. Porter, J.W. Ager, R.O. Ritchie, T. Alliston, Osteopontin deficiency increases bone fragility but preserves bone mass, Bone 46 (6) (2010) 1564–1573.
[56] P.J. Thurner, O.L. Katsamenis, The role of nanoscale toughening mechanisms in osteoporosis, Curr. Osteoporosis Rep. 12 (3) (2014) 351–356.
[57] M.E. Lyons, Transport and kinetics in electroactive polymers, in: I. Prigogine, S. A. Rice (Eds.), Advances in Chemical Physics, vol. 94. Polymeric Systems, Wiley, New York, 1996, pp. 297–624. Ch. 4.
[58] A. Abhilash, B.M. Baker, B. Trappmann, C.S. Chen, V.B. Shenoy, Remodeling of fibrous extracellular matrices by contractile cells: predictions from discrete fiber network simulations, Biophys. J. 107 (8) (2014) 1829–1840.
[59] H. Wang, A. Abhilash, C.S. Chen, R.G. Wells, V.B. Shenoy, Long-range force transmission in fibrous matrices enabled by tension-driven alignment of fibers, Biophys. J. 107 (11) (2014) 2592–2603.
[60] G. Subramanian, C.R. Picu, Mechanics of three-dimensional, nonbonded random fiber networks, Phys. Rev. E 83 (5) (2011) 056120.
[61] M. Aghvami, V. Barocas, E. Sander, Multiscale mechanical simulations of cell compacted collagen gels, J. Biomech. Eng. 135 (7) (2013) 071004.
[62] X. Ma, M.E. Schickel, M.D. Stevenson, A.L. Sarang-Sieminski, K.J. Gooch, S.N. Ghadiali, R.T. Hart, Fibers in the extracellular matrix enable long-range stress transmission between cells, Biophys. J. 104 (7) (2013) 1410–1418.
[63] E. Batschelet, Circular Statistics in Biology, Academic Press, New York, 1981.
[64] D. Hull, T. Clyne, An introduction to Composite Materials, Cambridge University Press, 1996.